bioRxiv preprint doi: https://doi.org/10.64898/2026.10.26.761989; this version posted October 28, 2026. The copyright holder for this preprint (which was not certified by peer review) is the author/funder, who has granted bioRxiv a license to display the preprint in perpetuity. It is made available under a CC-BY-NC 4.0 International license.

Three-Dimensional Fluid-Structure Interaction Reveals Trade-offs Among Oxygen Delivery, Shear, and Washout in Pediatric Roller-Pump Cardiopulmonary Bypass

Yunpeng Tu, MS[1,2,3], Yi-Ting Yeh, PhD[1,2,3], Alex de Lecea, MS[1], Kevin Charette, BA, CCP[4], Lyubomyr Bohuta, MD, PhD[5,6], Vishal Nigam, MD[2,3,7,8,9], Juan C. del Álamo, PhD[1,2,3,9], Christina L. Greene, MD[1,10,11]

[1]Department of Mechanical Engineering, University of Washington, Seattle, Washington; [2]Center for Cardiovascular Biology, University of Washington, Seattle, Washington; [3]Institute of Stem Cell and Regenerative Medicine Cardiovascular Biology, University of Washington, Seattle, Washington; [4]Heart Center, Seattle Children's Hospital, Seattle, Washington; [5]Congenital Cardiac Surgery, Seattle Children's Hospital, Seattle, Washington; [6]Division of Cardiothoracic Surgery, Department of Surgery, University of Washington, Seattle, Washington; [7]Department of Pediatrics (Cardiology), Seattle Children's Hospital, Seattle, Washington; [8]Center for Developmental Biology and Regenerative Medicine, Seattle Children's Research Institute, Seattle, Washington; [9]Division of Cardiology, Department of Pediatrics, University of Washington School of Medicine, Seattle, Washington; [10]Department of Surgery, University of California, Los Angeles, Los Angeles, California; [11]Cardiac Surgery, Children's Hospital of Orange County, Orange, California

Disclosure Statement

The authors have no conflicts of interest to disclose.

Funding Statement

This work was supported by the National Institutes of Health under grants R01HD106628 and R01HL170607 and by the Heart Center, Division of Pediatrics, Seattle Children's Hospital, Seattle, WA.

bioRxiv preprint doi: https://doi.org/10.64898/2026.10.26.761989; this version posted October 28, 2026. The copyright holder for this preprint (which was not certified by peer review) is the author/funder, who has granted bioRxiv a license to display the preprint in perpetuity. It is made available under a CC-BY-NC 4.0 International license.

Institutional Review Board Statement

Institutional review board approval was not required because this study involved computational simulations without human participants or identifiable patient data.

Glossary of Abbreviations and Symbols

APDL: Ansys Parametric Design Language

CFD: Computational fluid dynamics

CFL: Courant-Friedrichs-Lewy

CPB: Cardiopulmonary bypass

DO_2: Oxygen delivery

DO_2i: Indexed oxygen delivery

FSI: Fluid-structure interaction

Hct: Hematocrit

MUSCL: Monotone Upstream-Centered Schemes for Conservation Laws

OSI: Oscillatory shear index

PISO: Pressure-Implicit with Splitting of Operators

PR75: 75^{th} percentile

PRESTO!: Pressure Staggering Option

PVC: Polyvinyl chloride

RBCs: Red blood cells

RP-CPB: Roller-pump cardiopulmonary bypass

rpm: Revolutions per minute

bioRxiv preprint doi: https://doi.org/10.64898/2026.10.26.761989; this version posted October 28, 2026. The copyright holder for this preprint (which was not certified by peer review) is the author/funder, who has granted bioRxiv a license to display the preprint in perpetuity. It is made available under a CC-BY-NC 4.0 International license.

RRT: Relative residence time

SIRS: Systemic inflammatory response syndrome

TAWSR: Time-averaged wall shear rate

TAWSS: Time-averaged wall shear stress

μRRT: Modified relative residence time

Ω: Roller rotational speed

ϕ: Tubing occlusion

$\underline{Q}$: Cycle-averaged volumetric flow rate

$\underline{S_{max}}$: Cycle-averaged peak shear rate

$\underline{\tau_{max}}$: Cycle-averaged peak shear stress

μ: Dynamic viscosity

τ_s: Flow shear stress

$\dot{\gamma}$: Shear rate

$\overline{\overline{D}}$: Strain-rate tensor

bioRxiv preprint doi: https://doi.org/10.64898/2026.10.26.761989; this version posted October 28, 2026. The copyright holder for this preprint (which was not certified by peer review) is the author/funder, who has granted bioRxiv a license to display the preprint in perpetuity. It is made available under a CC-BY-NC 4.0 International license.

Central Message

Comparable levels of oxygen delivery across pediatric roller-pump cardiopulmonary bypass settings can conceal markedly different flow shear and washout environments.

Perspective Statement

Pediatric bypass strategies vary, and their mechanical effects remain incompletely understood. Three-dimensional fluid–structure interaction simulations link operating conditions to hemodynamics, flow shear, and washout, revealing different biomechanical environments at similar oxygen delivery. This platform enables evaluation of perfusion trade-offs to inform strategies for reducing blood trauma.

ABSTRACT

Objective: To determine how roller speed, tubing occlusion, and hematocrit jointly regulate oxygen delivery, shear, and washout in pediatric roller-pump cardiopulmonary bypass.

Methods: A three-dimensional, closed-loop fluid-structure interaction model resolved roller-tube contact, tubing deformation, and blood flow. Forty simulations combined 4 roller speeds (38-95 revolutions per minute), 2 occlusion levels (77% and 83%), and 5 hematocrit levels (15%-50%). Cycle-averaged flow, oxygen delivery, peak shear stress, and viscosity-normalized relative residence time were quantified.

Results: Roller compression produced retrograde leakage through the occluded gap, localized peak shear stress exceeding 100 pascals, and adjacent stagnation and recirculation. Flow increased nearly linearly with roller speed and was higher at greater occlusion, with little hematocrit dependence. Higher speed and occlusion increased peak shear stress while reducing relative residence time; higher hematocrit further increased peak shear stress. Similar oxygen delivery could arise from substantially different flow environments: among 10 conditions

bioRxiv preprint doi: https://doi.org/10.64898/2026.10.26.761989; this version posted October 28, 2026. The copyright holder for this preprint (which was not certified by peer review) is the author/funder, who has granted bioRxiv a license to display the preprint in perpetuity. It is made available under a CC-BY-NC 4.0 International license.

providing oxygen delivery of approximately 9-12 milliliters per minute, peak shear stress ranged from approximately 25 to 70 pascals. Within conditions satisfying an illustrative minimum oxygen-delivery threshold, lower hematocrit permitted speed and occlusion settings yielding lower peak shear stress and relative residence time.

Conclusions: Pediatric roller-pump settings that provide similar oxygen delivery can expose blood to markedly different shear and washout environments. Joint evaluation of these metrics may guide selection of speed, occlusion, and hematocrit to meet a target oxygen delivery while reducing shear and improving washout.

Keywords: Cardiopulmonary bypass; roller pump; pediatric cardiac surgery; fluid-structure interaction; shear stress; relative residence time

bioRxiv preprint doi: https://doi.org/10.64898/2026.10.26.761989; this version posted October 28, 2026. The copyright holder for this preprint (which was not certified by peer review) is the author/funder, who has granted bioRxiv a license to display the preprint in perpetuity. It is made available under a CC-BY-NC 4.0 International license.

INTRODUCTION

Approximately 40,000 children receive open-heart surgery yearly in the US, requiring cardiopulmonary bypass (CPB) for circulatory and respiratory support[1]. Roller pump-based CPB remains the dominant method for pediatric cases due to its compatibility with small circuits and low priming volume[2]. Despite its indispensable role, CPB is associated with serious postoperative complications, including systemic inflammatory response syndrome and multi-organ dysfunction[3,4]. Multiple factors have been implicated in these adverse outcomes, including blood contact with artificial surfaces, temperature modulation, ischemia-reperfusion injury, transfusion exposure, and excessive mechanical stress on circulating cells[5–11]. Supraphysiological flow shear is increasingly recognized as a contributor to CPB- or mechanical circulatory support- associated morbidity via hemolysis, platelet activation, and pro-inflammatory leukocyte activation[12–17]. Recent mechanobiology studies showed that monocytes exposed to CPB-relevant shear upregulate inflammatory pathways[13,14,16,17].

Current CPB operation focuses on maintaining adequate indexed oxygen delivery (DO_2i) to prevent ischemic injury, such as acute kidney injury, while minimizing clinically observable complications. Yet reported safe DO_2i thresholds vary across pediatric cohorts[18–22], and target hematocrit (Hct) remains controversial: Jonas and colleagues identified a threshold near 23.5%[23–25], whereas other studies support diverse strategies[26–29]. Moreover, roller-pump performance cannot be characterized by peak flow or oxygen delivery alone. In practice, oxygen transport is regulated by adjusting pump speed, Hct, and occlusion. These parameters, along with other circuit parameters such as tubing diameter, shape the stresses experienced by circulating cells. Thus, similar oxygen delivery indices may mask distinct, incompletely characterized biomechanical insults. From a mechanical perspective, roller-pump CPB is a high-occlusion form of peristaltic pumping, a classical transport mechanism in which a traveling compression wave displaces fluid through a deformable conduit[30]. The advancing

bioRxiv preprint doi: https://doi.org/10.64898/2026.10.26.761989; this version posted October 28, 2026. The copyright holder for this preprint (which was not certified by peer review) is the author/funder, who has granted bioRxiv a license to display the preprint in perpetuity. It is made available under a CC-BY-NC 4.0 International license.

wave generates transient and spatially localized tubing deformation, flow acceleration, and elevated shear stress[31–33]. It may also create disturbed transport regions characterized by recirculation and inefficient washout, exposing circulating blood cells to prolonged unphysiological flow in addition to short bouts of elevated shear[34,35]. Despite their potential biomechanical relevance, shear and transport-related metrics are rarely incorporated into perfusion decision-making.

Computational modeling offers a promising approach to investigating unphysiological flow stresses in CPB roller-pump circuits[31–33,36,37]. Existing studies follow two approaches: lumped-parameter models[36,37], which capture circuit-level pressure and flow-rate waveforms but lack spatial resolution, and computational fluid dynamics (CFD) analyses[31–33], which resolve local flow structures, but largely rely on two-dimensional domains with simplified models of tubing deformation. Neither approach captures the three-dimensional interaction among roller motion, tubing deformation, and flow. In addition, the combined effects of roller speed, occlusion, and hematocrit have not been systematically examined. Consequently, how these parameters jointly regulate oxygen delivery and flow-mediated insults remains poorly understood.

Three-dimensional fluid-structure interaction (FSI) analysis can feasibly resolve coupled roller-tube contact, deformation, and flow in roller pumps[38]. However, its potential for analyzing and optimizing CPB operation has not been realized yet. Here, we developed a three-dimensional FSI model of a pediatric roller-pump CPB circuit and conducted a systematic campaign of simulations varying the operating conditions. Our analysis identifies operating strategies that balance oxygen transport and biomechanical insults such as shear exposure, and disturbed washout.

bioRxiv preprint doi: https://doi.org/10.64898/2026.10.26.761989; this version posted October 28, 2026. The copyright holder for this preprint (which was not certified by peer review) is the author/funder, who has granted bioRxiv a license to display the preprint in perpetuity. It is made available under a CC-BY-NC 4.0 International license.

METHODS

Roller pump computational model

Figure 1 situates the computational model within a representative CPB circuit (Fig. 1A) and shows the LivaNova S5 pump head on which it was based (Fig. 1B). The pump comprised a 150-mm-diameter raceway, two opposing 30.5-mm-diameter rollers with adjustable occlusion, outlet tubing clamps, and eight cylindrical guides (four per side). A 0.09-mm clearance between the guides and tubing outer wall prevented out-of-plane displacement. During each 360° rotation, every tubing section was compressed twice, once by each roller.

The system was modeled in Ansys 2022 R2 using a solid domain for the pump assembly and tubing, and a fluid domain for the circulating fluid. The solid domain comprised the backplate (gray), dual-roller assembly and guides (brown), and tubing (green, blue; Fig. 1C). The tubing inner diameter matched the nominal clinical size (4.76 mm), whereas its outer diameter (6.35 mm) followed commercially available flexible PVC tubing. The tubing was divided into a deformable raceway segment (green) and a fixed segment (blue) connecting the downstream and upstream ends of the raceway to form a closed loop, while the fixed segment represented the tubing immobilized by the pump clamps. The two segments, of lengths 400 mm (green) and 263 mm (blue), were joined by bonded interfaces (Fig. 1C-ii). The fluid domain occupied the tubing lumen and formed the same closed loop, allowing roller-induced deformation to generate flow without prescribed inlet or outlet conditions.

Fluid-structure interaction simulation framework

Roller-induced tubing deformation was simulated with the Transient Structural module in Ansys Mechanical APDL. To transition smoothly to steady operation, the rigid roller assembly was prescribed three successive motions: translation toward the tubing to establish the target occlusion (initial engagement, $0<t<0.4$ s); a linear increase in angular speed from rest to the

bioRxiv preprint doi: https://doi.org/10.64898/2026.10.26.761989; this version posted October 28, 2026. The copyright holder for this preprint (which was not certified by peer review) is the author/funder, who has granted bioRxiv a license to display the preprint in perpetuity. It is made available under a CC-BY-NC 4.0 International license.

prescribed value (rotation ramp, 0.4<t<3.4 s); and constant-speed rotation thereafter (t>3.4 s; Supplementary Fig. 1).

The deformable tubing was modeled as an isotropic, linearly elastic material (Young's modulus, 40 MPa; Poisson's ratio, 0.48; density, 1500 kg·m^{-3})[39,40]. The tubing was discretized using the MultiZone method with quadratic 20-node hexahedra and quadratic wedges as required in curved regions. A nominal 0.8-mm element size yielded 98,067 nodes and 15,840 elements. One quadratic element was used through the wall because the analysis targeted global lumen deformation rather than through-thickness stresses. Frictionless contact was imposed at the tubing-roller, tubing-guide, and tubing-backplate interfaces.

One-way fluid-structure interaction (FSI) was implemented using ANSYS System Coupling through a surface-to-surface interface between the inner surface of the deformable tubing and the corresponding fluid-domain boundary. The fixed tubing segment was excluded from coupling. At each coupling step, tubing-wall nodal displacements were transferred from the structural solver to a System Coupling dynamic-mesh boundary in Fluent. A two-way FSI simulation confirmed that flow-induced pressure gradients negligibly affected tubing deformation, supporting the one-way approximation. The structural and fluid solvers were synchronized using identical time steps.

Computational fluid dynamics model

Flow was simulated in ANSYS Fluent 2022 R2 using a transient, three-dimensional, finite-volume formulation under the assumptions of incompressible, Newtonian flow governed by the Navier-Stokes and continuity equations. A no-slip boundary condition was imposed at the tubing wall, whose motion was prescribed through the FSI coupling. The closed-loop tubing geometry enabled the flow to be solved without prescribed inlet or outlet boundary conditions. No turbulence model was used.

bioRxiv preprint doi: https://doi.org/10.64898/2026.10.26.761989; this version posted October 28, 2026. The copyright holder for this preprint (which was not certified by peer review) is the author/funder, who has granted bioRxiv a license to display the preprint in perpetuity. It is made available under a CC-BY-NC 4.0 International license.

The fluid domain (Figure 1C, right) was discretized using an unstructured tetrahedral mesh with a nominal element size of 0.4 mm, yielding 304,542 nodes and 1,596,693 elements. Transferred wall motion was propagated using Spring/Laplace/Boundary Layer smoothing and implicit local cell- and face-based remeshing, with a residual criterion of 10^{-5}, length scales of 0.24-0.59 mm, and maximum cell and face skewness values of 0.79 and 0.57, respectively. The mesh provided approximately 47 elements across the undeformed tubing and 12 across the maximally occluded section.

Convective terms were discretized with third-order MUSCL, using PRESTO! pressure interpolation and PISO pressure-velocity coupling; time integration was second-order implicit. Up to 30 nonlinear iterations were performed per time step, with convergence defined by scaled residuals below 10^{-6} for continuity and 10^{-5} for momentum. A 0.0004-s step was used during roller engagement and the rotation ramp ($t<3.4$ s) and during subsequent flow development until flow rate and domain-averaged and peak shear stress became periodic. This required 3, 4, 6, and 7 cycles at 38, 57, 76, and 95 rpm, respectively. The step was then reduced to 0.00025 s for an additional 1.4 pump cycles, and metrics were calculated over the final complete cycle. The Courant-Friedrichs-Lewy (CFL) number remained below 0.4 throughout the domain except for the occlusion region, where it averaged 2.2.

Mesh and time-step sensitivity were evaluated at 83% occlusion, 50% hematocrit, and 95 rpm. Nominal element sizes of 1.2, 1.0, 0.8, 0.6, 0.4, and 0.3 mm were tested. Time steps were scaled proportionally to element size to maintain comparable CFL numbers. Relative to the 0.3-mm reference, differences for the 1.2-, 1.0-, 0.8-, 0.6-, and 0.4-mm meshes were [8.71, 8.4, 7.17, 5.31, and 2.47] % in flow rate and [58.65, 45.61, 31.69, 24.88, and 2.91] % in peak shear stress. Simulations with dt = 0.0000625, 0.000125, 0.00025, 0.0005, and 0.001 s were then compared under the same condition. Relative to the reference simulation with dt = 0.0000625, differences for dt = 0.000125, 0.00025, 0.0005, and 0.001 s were [0.08, 3.37, 8.99, and 10.38]

bioRxiv preprint doi: https://doi.org/10.64898/2026.10.26.761989; this version posted October 28, 2026. The copyright holder for this preprint (which was not certified by peer review) is the author/funder, who has granted bioRxiv a license to display the preprint in perpetuity. It is made available under a CC-BY-NC 4.0 International license.

% in flow rate and [3.26, 3.52, 10.21, and 20.99] % in peak shear stress. Based on these results, the 0.4-mm mesh and 0.00025-s time step were selected for final simulations.

All simulations were performed on the Hyak high-performance computing cluster at the University of Washington.

Operating parameter space

Roller occlusion was defined as

$$\phi = \left(1 - \frac{h}{2r}\right) \times 100\ [\%]$$

where h is the minimum lumen gap prescribed during roller engagement and r is the undeformed tubing inner radius. Two occlusion levels were prescribed: ϕ= 77% and 83%, corresponding to h ≈1.1 and 0.8 mm. Four constant roller speeds (Ω = 38, 57, 76, and 95 rpm) were investigated. For each pair of ϕ and Ω values, five hematocrit (Hct) levels ranging from 15% to 50% were considered. Blood density was fixed at 1060 kg·m^{-3} as its Hct dependence was negligible compared with that of viscosity.

Hematocrit-dependent viscosity (μ units: mPa·s) values were determined from Long et al.'s empirical regression[41] for pediatric blood under an oscillatory strain of 5, with Hct expressed as a percentage: $\mu=2.58+4.211\times10^{-4}Hct^{2.36}$

Post-processing

Flow visualization and data extraction were performed using Ansys CFD-Post 2022 R2, and Secondary analyses and associated graphs were performed with MATLAB R2022b.

Assuming total oxygen saturation, a hemoglobin concentration linearly proportional to Hct, and neglecting the small contribution from dissolved oxygen, oxygen delivery[19] (DO_2, units: mL·min^{-1}) was determined from the cycle-averaged flow rate $\underline{Q}$ (L·min^{-1}) and hematocrit as $DO_2 = 4.624\ \underline{Q}\ Hct$.

bioRxiv preprint doi: https://doi.org/10.64898/2026.10.26.761989; this version posted October 28, 2026. The copyright holder for this preprint (which was not certified by peer review) is the author/funder, who has granted bioRxiv a license to display the preprint in perpetuity. It is made available under a CC-BY-NC 4.0 International license.

Flow shear stress (τ_s) was calculated as the product of the dynamic viscosity (μ) and the shear-rate ($\dot{\gamma}$), $\tau_s = \mu\dot{\gamma} = \mu\sqrt{2\bar{\bar{D}}:\bar{\bar{D}}}$, where $\bar{\bar{D}}$ is the strain-rate tensor, defined as the symmetric part of the velocity gradient tensor. At each time point, the maxima of $\dot{\gamma}$ and τ_s were identified within the fluid domain. Then, the cycle-averaged peak shear rate ($\underline{S}_{max}$) and stress ($\underline{\tau}_{max}$) were calculated as the time average of these spatial maxima.

Relative residence time (RRT; units: Pa^{-1}) is usually defined as

$$RRT = \frac{1}{(1-2\ OSI)\ TAWSS},$$

where OSI and $TAWSS$ denote the oscillatory shear index and time-averaged wall shear stress[42,43]. Because blood viscosity varies with Hct in our study, we used the modified RRT (μRRT; units: s)

$$\mu RRT = \frac{\mu}{(1-2\ OSI)\ TAWSS} = \frac{1}{(1-2\ OSI)\ TAWSR}$$

where $TAWSR$ (units: s^{-1}) is the time-averaged wall shear rate, $TAWSR = TAWSS/\mu$. Elevated μRRT corresponds to near-wall regions experiencing recirculation and reduced washout. To characterize RRT variation along the raceway while reducing sensitivity to isolated extreme values, we reported the 75th percentile of the μRRT at each position.

RESULTS

Roller compression generates high shear, backflow, and recirculation

To examine how CPB operating conditions may affect circulating cells, we analyzed tubing deformation and intraluminal flow across combinations of roller speed (Ω), occlusion (ϕ), and hematocrit (Hct). Figure 2 illustrates roller-induced deformation, localized flow shear, and altered blood transport at peak shear for the case with the highest occlusion, hematocrit, and roller speed ($\phi = 83\%$, Hct=50%, $\Omega = 95$ rpm).

bioRxiv preprint doi: https://doi.org/10.64898/2026.10.26.761989; this version posted October 28, 2026. The copyright holder for this preprint (which was not certified by peer review) is the author/funder, who has granted bioRxiv a license to display the preprint in perpetuity. It is made available under a CC-BY-NC 4.0 International license.

Peak shear stress occurred when the roller compressed the tubing approximately 11° from the top of the raceway during counterclockwise rotation. At this timepoint, the tubing's circular cross-section was bent and flattened into the obround shape as shown in Figure 2A inset, widening laterally from its nominal radius of r=3.175 mm to r=4.317 mm. The resulting three-dimensional deformation of the tubing wall reached maximum local elastic strain values of approximately 0.5. Moreover, because the tubing was not fixed to the backplate, the entire tubing displaced within the raceway, in line with operating-room observations (Supplementary Movie 1). These features are typically not captured by previous two-dimensional computational models of roller pumps[31–33].

Figure 2B shows the cross-sectional velocity field and inset profiles across the occluded gap and free tubing, with transverse position normalized by the nominal tubing diameter. At 83% occlusion, the gap produced a sharply peaked profile with a maximum velocity of 1.545 m/s, approximately four times the free-tube value (0.334 m/s), where the profile was broader and symmetric. The free-tube velocity agreed with previous computational studies[31–33], which is notable given that it emerged from the closed-loop pump-circuit dynamics rather than being prescribed via inflow/outflow boundary conditions. The Reynolds number was Re=266, which was below reported values (500-1400) consistent with our smaller pediatric circuit. Peak gap velocity was near the lower end of previous reports[31–33], likely because the prior studies used greater normalized occlusion in larger tubing[32,33] and two-dimensional domains that prevented lateral widening of the compressed lumen.

Localized acceleration through the occluded gap concentrated shear stress in the roller-compressed region (Figure 2C), where it exceeded 100 Pa versus approximately 2 Pa in most of the remaining tubing. These values agreed with some previous studies[32,33] but were below those reported by Mulholland et al.[31], consistent with the peak-velocity differences above.

bioRxiv preprint doi: https://doi.org/10.64898/2026.10.26.761989; this version posted October 28, 2026. The copyright holder for this preprint (which was not certified by peer review) is the author/funder, who has granted bioRxiv a license to display the preprint in perpetuity. It is made available under a CC-BY-NC 4.0 International license.

Flow through the occluded gap reversed relative to the net flow direction (Figure 2D), while the flattened lumen produced lateral expansion and convergence of the instantaneous streamlines. This three-dimensional pattern created a stagnation region on the counterclockwise side and a recirculation region on the clockwise side of the occlusion, consistent with flow trapping and prolonged residence time. Reversed flow and trapping are characteristic features of high-occlusion peristaltic pumping[30].

All simulations exhibited similar disturbed flow patterns, with only modest case-to-case variations. At high occlusion, hematocrit, and roller speed ($\phi = 83\%$, Hct=50%, $\Omega = 95$ rpm; Figure 2Di), stronger net forward flow rapidly realigned streamlines on both sides of the roller, confining disturbances to a small region. At low occlusion and roller speed ($\phi = 77\%$, Hct=50%, $\Omega = 38$ rpm; Figure 2Dii), weaker forward flow produced a larger recirculation region.

Roller speed, occlusion, and hematocrit differentially regulate oxygen delivery and shear generation

We examined how roller speed, occlusion, and hematocrit jointly regulate oxygen delivery (DO_2), cycle-averaged flow rate ($\underline{Q}$), peak shear rate ($\underline{S}_{max}$), and peak shear stress ($\underline{\tau}_{max}$) across 40 simulations (Figure 3). The campaign included two occlusion levels (ϕ =77% and 83%), four roller speeds ($\Omega = 38$, 57, 76, and 95 rpm), and five hematocrit levels (Hct=15-50%). Because roller speed is the primary parameter adjusted during CPB, results are plotted against speed, with each curve representing fixed hematocrit and occlusion.

Figure 3A shows that $\underline{Q}$ increased almost linearly with Ω over the investigated rpm range. This behavior is consistent with classical low-Reynolds-number peristaltic pumping theory, which predicts $Q \sim r^2 R_p \Omega f(\phi)$, where r is the inner tubing radius, R_p the pump radius, and the occlusion factor $f(\phi)$ increases from 0 to 1 as ϕ increases from 0 to 100%. The theory also

bioRxiv preprint doi: https://doi.org/10.64898/2026.10.26.761989; this version posted October 28, 2026. The copyright holder for this preprint (which was not certified by peer review) is the author/funder, who has granted bioRxiv a license to display the preprint in perpetuity. It is made available under a CC-BY-NC 4.0 International license.

307 includes a negative correction associated with viscously dominated backflow through the
308 occlusion[35]. As ϕ approaches complete occlusion, this correction vanishes, making $\underline{Q}$
309 independent of fluid viscosity. Accordingly, increasing ϕ in our simulations increased the
310 slope of the $\underline{Q}$-rpm relationship, whereas hematocrit exerted only a minor influence. The weak
311 dependence of $\underline{Q}$ on hematocrit suggests that the operating conditions were in the high-
312 occlusion regime, where viscous backflow is small. The predicted flow rates were also
313 consistent with previous simulations[31–33].

314 Hematocrit was a significant determinant of oxygen delivery (Figure 3B), producing
315 greater separation among the DO_2 vs. rpm curves than among the flow-rate curves. Importantly,
316 overlap among these curves showed that comparable oxygen delivery could be achieved
317 through different parameter combinations; for example, 20% hematocrit at $\phi = 83\%$ produced
318 nearly the same DO_2 vs. rpm relationship as 40% hematocrit at $\phi = 77\%$. Thus, alternative
319 operating strategies could achieve the same oxygen-delivery target while generating different
320 shear environments, potentially allowing biomechanical insult to be minimized.

321 To determine whether these alternative operating strategies produced different shear
322 environments, we examined peak shear rate and stress. $\underline{S}_{max}$ increased with roller speed and
323 occlusion (Figure 3C), reflecting faster backflow and steeper velocity gradients, respectively.
324 It varied little across lower Hct values but tended to decrease at higher Hct because increased
325 viscosity resisted backflow through the occlusion. A similar dependence on Ω and ϕ was
326 observed for $\underline{\tau}_{max}$ (Figure 3D), but its hematocrit dependence was reversed. Because shear
327 stress scales with the product of viscosity and shear rate, the increase in viscosity at higher Hct
328 outweighed the reduction in $\underline{S}_{max}$, resulting in higher $\underline{\tau}_{max}$.

329 **Shear exposure at a given flow or oxygen delivery depends on pump operating strategy**

bioRxiv preprint doi: https://doi.org/10.64898/2026.10.26.761989; this version posted October 28, 2026. The copyright holder for this preprint (which was not certified by peer review) is the author/funder, who has granted bioRxiv a license to display the preprint in perpetuity. It is made available under a CC-BY-NC 4.0 International license.

We compared shear generation across operating conditions to determine whether CPB settings could reduce shear while maintaining flow or oxygen-delivery targets. Peak shear rate generally increased with cycle-averaged flow (Figure 4A), but differences in occlusion and hematocrit produced substantial variation in $\underline{S}_{max}$ at a given $\underline{Q}$. For example, at $\underline{Q}$ ≈1.5 cm^3/s, $\underline{S}_{max}$ ranged from approximately 1.0 to 1.7 × 10^4 s^{-1} across the simulated operating conditions.

Accounting for hematocrit-dependent oxygen-carrying capacity and viscosity produced a more complex relationship between oxygen delivery and peak shear stress (Figure 4B). As with flow rate, similar oxygen delivery (DO_2) could arise from multiple operating conditions associated with markedly different peak shear stresses. For example, ten conditions yielded DO_2 values between approximately 9 and 12 mL/min, yet $\underline{\tau}_{max}$ ranged from approximately 25 to 70 Pa—a nearly threefold difference over a relatively narrow oxygen-delivery range. Conversely, comparable peak shear stresses occurred across a wide range of oxygen delivery: seven conditions produced $\underline{\tau}_{max}$ values between 70 and 80 Pa while DO_2 ranged from approximately 12 to 25 mL/min.

The reduced spread at DO_2 values above approximately 20 mL/min should not be interpreted as convergence of the oxygen delivery-peak shear stress relationship. Instead, it reflects sparse sampling of the operating space at higher oxygen delivery, which was reached by only a few parameter combinations. Additional cases with higher occlusion and/or pump speeds would likely populate this region and reveal a wider range of peak shear stresses at comparable oxygen delivery, extending the trend observed at lower DO_2.

Peak shear stress alone does not capture the unphysiological recirculation and stagnation on either side of the roller occlusion (Figure 2D). We therefore quantified these disturbances using modified relative residence time (μRRT), a metric combines wall shear magnitude and directional oscillation, that characterizes prolonged residence and poor washout near walls[43].

bioRxiv preprint doi: https://doi.org/10.64898/2026.10.26.761989; this version posted October 28, 2026. The copyright holder for this preprint (which was not certified by peer review) is the author/funder, who has granted bioRxiv a license to display the preprint in perpetuity. It is made available under a CC-BY-NC 4.0 International license.

Figures 5A-B show full-cycle μRRT distributions for representative high-occlusion/high-speed and low-occlusion/low-speed cases from Figure 2D. Because they span the full roller cycle, these maps describe cumulative transport, and elevated μRRT indicates longer residence inside the recirculating regions. In both cases, elevated values were concentrated within the raceway above the gray dashed line, whereas μRRT was substantially lower in the free tubing.

Within the raceway, μRRT depended on roller-contact state. Values were highest in the upper raceway, where one roller compressed the tubing during part of the cycle, and lower in the lateral raceway, where both rollers compressed it from opposite sides, although they remained above free-tubing values. Spatial patterns were similar across operating conditions, but magnitudes differed substantially. Maximum μRRT in the low-speed, low-occlusion case ($\phi = 77\%$, Hct=50%, $\Omega = 38$ rpm) was approximately 2.5-fold higher than in the high-speed, high-occlusion case ($\phi = 83\%$, Hct=50%, $\Omega = 95$ rpm).

Figure 5C summarizes these effects by plotting the 75th percentile of μRRT against roller speed for all occlusion-hematocrit combinations. μRRT decreased with increasing speed and occlusion, indicating improved washout. Hematocrit had a stronger effect for ϕ =77% than for $\phi = 83\%$, with lower values generally reducing μRRT through viscosity-dependent changes in the flow.

Lower hematocrit permits favorable shear-residence-time trade-offs under an oxygen-delivery constraint

Because peak shear stress and relative residence time responded differently to operating conditions, we evaluated them jointly by plotting $\underline{\tau}_{max}$ against the 75th percentile of μRRT (PR75) across all simulations (Figure 6A). Lower PR75 μRRT generally coincided with higher $\underline{\tau}_{max}$, revealing a trade-off between washout and shear. This relationship depended strongly on

bioRxiv preprint doi: https://doi.org/10.64898/2026.10.26.761989; this version posted October 28, 2026. The copyright holder for this preprint (which was not certified by peer review) is the author/funder, who has granted bioRxiv a license to display the preprint in perpetuity. It is made available under a CC-BY-NC 4.0 International license.

hematocrit: lower-Hct curves shifted toward lower $\underline{\tau}_{max}$ and PR75 μRRT, closer to the lower-left region where both metrics are minimized.

To determine whether the favorable shift at lower hematocrit persisted after accounting for the concomitant reduction in oxygen delivery, we imposed an illustrative threshold of $DO_2 \geq 7$ mL/min, selected to retain sufficient coverage of the simulated parameter space rather than to represent a clinically relevant target. The filter excluded cases with insufficient oxygen transport, shown in light gray in Figure 6B. Among the retained cases, lower-Hct conditions remained closest to the low-shear, low-residence-time region. Thus, lower hematocrit permitted occlusion and pump speed to be adjusted toward lower shear and residence time while remaining above the illustrative oxygen-delivery threshold.

DISCUSSION

Cardiopulmonary bypass (CPB) is associated with postoperative complications, including systemic inflammatory response syndrome (SIRS) and multiorgan dysfunction[3,4]. Proposed contributors include blood contact with artificial surfaces, temperature changes, ischemia-reperfusion injury, nonpulsatile flow, transfusion, hemolysis, and supraphysiological shear stress[3–11].

Maintaining adequate oxygen delivery (DO_2) is a central goal of CPB, yet proposed nadir indexed oxygen delivery (DO_2i) thresholds for limiting acute kidney injury vary from 258 to 400 mL/min/m² across adult and pediatric cohorts, depending on patient age and phase of bypass[18–22]. Reported hematocrit (Hct) targets are similarly heterogeneous. Two randomized infant trials compared lower and higher hematocrit strategies during hypothermic CPB[23,24]. A pooled analysis of these trials found that psychomotor scores increased with hematocrit up to 23.5% and plateaued above that level[25]. Adult studies associated thresholds of 23% and 24% with renal failure and low-output syndrome, respectively[26]. High-flow/high-Hct pediatric

bioRxiv preprint doi: https://doi.org/10.64898/2026.10.26.761989; this version posted October 28, 2026. The copyright holder for this preprint (which was not certified by peer review) is the author/funder, who has granted bioRxiv a license to display the preprint in perpetuity. It is made available under a CC-BY-NC 4.0 International license.

401 protocols (200 mL/kg/min, >32%) were associated with lower acute kidney injury and acute
402 neurological event rates than conventional conditions (150 mL/kg/min, >25%)[27,28]. Conversely,
403 Reagor et al. reported a lower nadir Hct in their high-flow than low-flow group (25% vs 28%)[29],
404 underscoring that flow and Hct cannot be considered independently.

405 This variability reflects institutional strategies that adjust hematocrit and flow primarily
406 to preserve oxygen delivery, with limited consideration of shear in the pump circuit. Studies
407 have shown that monocytes exposed to CPB-related shear stress upregulate inflammatory
408 cytokines, particularly within the high-shear environment of the pump raceway[13,14,16,17]. More
409 broadly, excessive shear has been linked to hemolysis, sublethal red blood cell damage, and
410 leukocyte and platelet activation[44–54]. Dextran-based priming strategies have also been reported
411 to reduce hemolysis, potentially by increasing the resistance of RBCs to shear compared to
412 crystalloid-based priming[55]. Together, these observations expose a major gap: no established
413 framework integrates oxygen-delivery and shear-related blood-injury criteria when selecting
414 CPB settings.

415 Roller pumps remain widely used in pediatric CPB because they enable compact, low-
416 prime circuits that limit hemodilution and transfusion exposure in infants and small children[2].
417 To date, comparative studies between roller and centrifugal pumps have not established clear
418 superiority of either pump type[56–59]. Roller-pump fluid mechanics have traditionally been
419 interpreted through classical studies of periodic peristaltic wave trains. These studies showed
420 that forward transport is accompanied by retrograde leakage through the residual gap and fluid
421 trapping near the moving constriction, with net flow governed by occlusion, wave speed,
422 pressure gradient, and viscosity[30,34,35]. Asymmetric and single-wave studies, which more
423 closely resemble roller-pump operation, confirmed these trends[60,61]. However, these idealized
424 models generally assume viscous-dominated flow and do not resolve the detailed flow

bioRxiv preprint doi: https://doi.org/10.64898/2026.10.26.761989; this version posted October 28, 2026. The copyright holder for this preprint (which was not certified by peer review) is the author/funder, who has granted bioRxiv a license to display the preprint in perpetuity. It is made available under a CC-BY-NC 4.0 International license.

generated by realistic three-dimensional tubing deformation, for which fluid inertia may not be negligible.

Only a few computational studies have examined flow within roller pumps used for CPB. Lumped-parameter models representing the pump as a series of interconnected compartments have been used to study pressure pulsations and their dependence on pump speed, occlusion, and downstream resistance[36,37]. However, such models cannot resolve local flow structures or shear stresses within the tubing. Computational fluid dynamics models have also been reported, but these relied on two-dimensional domains reconstructed from photographed tubing profiles or prescribed using simplified geometries[31–33]. A three-dimensional FSI model was previously presented for a generic peristaltic pump[38]. In this framework, tubing deformation and the resulting flow field emerge from the coupled roller-tube-fluid dynamics rather than from a prescribed lumen geometry or inlet waveform. However, that study demonstrated feasibility rather than systematically evaluating CPB-relevant hemodynamics.

To our knowledge, this is the first pediatric CPB study to combine three-dimensional roller-tube FSI with a closed-loop circuit and systematically vary roller speed, occlusion, and hematocrit. Our three-dimensional simulations reproduced the principal flow features reported in previous two-dimensional models, including strong acceleration and elevated shear within the occluded gap, retrograde leakage beneath the roller, and substantial changes in the local flow as the rollers entered and left the raceway[31–33]. Previous studies prescribed two-dimensional compressed-lumen geometries, whereas our model captured lateral widening of the flattened tubing, partially preserving the occluded flow area and likely contributing to lower peak velocities. Our configuration also operated at lower Reynolds numbers than the previously modeled systems, consistent with the smaller tubing dimensions of pediatric CPB. Although

bioRxiv preprint doi: https://doi.org/10.64898/2026.10.26.761989; this version posted October 28, 2026. The copyright holder for this preprint (which was not certified by peer review) is the author/funder, who has granted bioRxiv a license to display the preprint in perpetuity. It is made available under a CC-BY-NC 4.0 International license.

two earlier studies used turbulence closures[32,33], sustained turbulence at their reported Reynolds numbers under pulsatile conditions remains uncertain.

An important implication of our simulations, together with prior studies, is that roller-pump operation generates spatially and temporally heterogeneous hemodynamic insults within the raceway tubing. Blood cells passing through the occluded gap experience brief supraphysiological shear, whereas those trapped in the adjacent recirculation regions may undergo poor washout and repeated exposures to disturbed flow. Peak shear stress and relative residence time provide complementary measures of these phenomena.

A central finding of this study is that a prescribed oxygen-delivery target does not define a unique roller-pump operating condition. Roller speed, occlusion, and hematocrit affected pump performance through distinct mechanisms: roller speed primarily regulated bulk flow, whereas hematocrit had comparatively little effect on flow rate but strongly influenced oxygen-carrying capacity and shear stress through its effect on blood viscosity. This interplay creates an opportunity to optimize CPB settings beyond oxygen delivery alone. However, shear and washout cannot generally be optimized simultaneously. For example, decreasing roller speed reduced peak shear but increased relative residence time.

Among the simulated conditions satisfying the oxygen-delivery constraint, lower hematocrit permitted roller speed and occlusion to be adjusted toward a more favorable balance of peak shear stress and relative residence time. This finding is relevant to the growing use of clear crystalloid priming and transfusion-sparing strategies in pediatric CPB[62–65]. Although clear priming is intended primarily to reduce allogeneic transfusion and its inflammatory burden, it may therefore provide an additional hemodynamic benefit.

This study has limitations. Numerical constraints on roller-tube contact limited achievable residual gaps to approximately 1 mm. In the smaller pediatric tubing, this corresponded to

bioRxiv preprint doi: https://doi.org/10.64898/2026.10.26.761989; this version posted October 28, 2026. The copyright holder for this preprint (which was not certified by peer review) is the author/funder, who has granted bioRxiv a license to display the preprint in perpetuity. It is made available under a CC-BY-NC 4.0 International license.

normalized occlusions of 77%-83%—below the approximately 90% modeled previously[31–33]—and yielded flow rates below typical clinical values. Direct comparison is further limited because clinical occlusion is rarely reported despite standardized retrograde-flow setting procedures[66]. Future models should extend to higher occlusions to determine whether the observed trends persist under clinically representative flow conditions.

Peak shear stress identifies the most intense local loading, but blood-cell injury depends on both shear magnitude and exposure duration[67]. We thus complemented peak shear stress with RRT to identify regions of poor washout and prolonged residence, but RRT is not a direct measure of cumulative cell damage. More mechanistic estimates would involve accumulating an empirically calibrated damage variable along cell trajectories[68–70].

The simplified closed-loop circuit, consistent with prior peristaltic models[71], generated flow from roller-induced tubing deformation without prescribed inlet or outlet conditions, while omitting the full tubing length and downstream hydraulic resistance. Separately, the model neglected frictional heating, tubing fatigue, and plasticizer leaching[72,73]. Although fatigue and failure are mainly associated with prolonged pumping or excessive occlusion[74,75], their dependence on roller speed and occlusion may impose additional optimization constraints.

CONCLUSION

To our knowledge, this is the first systematic three-dimensional FSI study of pediatric roller-pump CPB across 40 combinations of roller speed, occlusion, and hematocrit. The simulations revealed localized high shear within the occluded gap and poor washout in adjacent recirculation regions. Different parameter combinations met similar oxygen-delivery targets while yielding distinct shear and washout environments. Lower hematocrit permitted selection of roller-speed and occlusion settings yielding lower peak shear stress and relative residence

bioRxiv preprint doi: https://doi.org/10.64898/2026.10.26.761989; this version posted October 28, 2026. The copyright holder for this preprint (which was not certified by peer review) is the author/funder, who has granted bioRxiv a license to display the preprint in perpetuity. It is made available under a CC-BY-NC 4.0 International license.

time. These findings support multimetric optimization of roller-pump operation and motivate future experimental validation under clinically representative conditions.

bioRxiv preprint doi: https://doi.org/10.64898/2026.10.26.761989; this version posted October 28, 2026. The copyright holder for this preprint (which was not certified by peer review) is the author/funder, who has granted bioRxiv a license to display the preprint in perpetuity. It is made available under a CC-BY-NC 4.0 International license.

REFERENCES

1. Pasquali SK, Thibault D, O'Brien SM, et al. National Variation in Congenital Heart Surgery Outcomes. *Circulation*. 2020;142(14):1351-1360. doi:10.1161/CIRCULATIONAHA.120.046962

2. Datt B, Nguyen MB, Plancher G, et al. The Impact of Roller Pump vs. Centrifugal Pump on Homologous Blood Transfusion in Pediatric Cardiac Surgery. *J Extra Corpor Technol*. 2017;49(1):36-43.

3. Warren OJ, Smith AJ, Alexiou C, et al. The Inflammatory Response to Cardiopulmonary Bypass: Part 1—Mechanisms of Pathogenesis. *J Cardiothorac Vasc Anesth*. 2009;23(2):223-231. doi:10.1053/j.jvca.2008.08.007

4. Larmann J, Theilmeier G. Inflammatory response to cardiac surgery: cardiopulmonary bypass versus non-cardiopulmonary bypass surgery. *Best Pract Res Clin Anaesthesiol*. 2004;18(3):425-438. doi:10.1016/j.bpa.2003.12.004

5. Karacaer F. Systemic inflammatory response syndrome in pediatric patients undergoing cardiac surgery. *J Cardıo-Vasc-Thoracıc Anaesthesıa Intensıve Care Socıety*. Published online 2023. doi:10.14744/GKDAD.2023.10438

6. Fudulu D, Angelini G. Oxidative Stress after Surgery on the Immature Heart. Perrone S, ed. *Oxid Med Cell Longev*. 2016;2016(1):1971452. doi:10.1155/2016/1971452

7. Boehne M, Sasse M, Karch A, et al. Systemic inflammatory response syndrome after pediatric congenital heart surgery: Incidence, risk factors, and clinical outcome. *J Card Surg*. 2017;32(2):116-125. doi:10.1111/jocs.12879

8. Durandy Y. Minimizing Systemic Inflammation During Cardiopulmonary Bypass in the Pediatric Population. *Artif Organs*. 2014;38(1):11-18. doi:10.1111/aor.12195

bioRxiv preprint doi: https://doi.org/10.64898/2026.10.26.761989; this version posted October 28, 2026. The copyright holder for this preprint (which was not certified by peer review) is the author/funder, who has granted bioRxiv a license to display the preprint in perpetuity. It is made available under a CC-BY-NC 4.0 International license.

9. Bronicki RA, Hall M. Cardiopulmonary Bypass-Induced Inflammatory Response: Pathophysiology and Treatment. *Pediatr Crit Care Med*. 2016;17(8):S272-S278. doi:10.1097/PCC.0000000000000759

10. O'Neil MP, Fleming JC, Badhwar A, Guo LR. Pulsatile Versus Nonpulsatile Flow During Cardiopulmonary Bypass: Microcirculatory and Systemic Effects. *Ann Thorac Surg*. 2012;94(6):2046-2053. doi:10.1016/j.athoracsur.2012.05.065

11. Kozik DJ, Tweddell JS. Characterizing the Inflammatory Response to Cardiopulmonary Bypass in Children. *Ann Thorac Surg*. 2006;81(6):S2347-S2354. doi:10.1016/j.athoracsur.2006.02.073

12. Lommel VC, Fahrenholz M, Kertzscher U, Lommel M, Kleine-Brueggeney M. Pediatric Versus Adult Shear-Induced Hemolysis: Are Age-Related Blood Properties the Main Cause for Differences? *Artif Organs*. 2026;50(5):721-729. doi:10.1111/aor.70100

13. Zhou H, Scatena M, Tu LN, Giachelli CM, Nigam V. Monocyte adhesion to and transmigration through endothelium following cardiopulmonary bypass shearing is mediated by IL-8 signaling. *Front Cardiovasc Med*. 2024;11:1454302. doi:10.3389/fcvm.2024.1454302

14. Tu LN, Hsieh L, Kajimoto M, et al. Shear stress associated with cardiopulmonary bypass induces expression of inflammatory cytokines and necroptosis in monocytes. *JCI Insight*. 2021;6(1):e141341. doi:10.1172/jci.insight.141341

15. Sun W, Han D, Awad MA, Leibowitz JL, Griffith BP, Wu ZJ. Role of thrombin to non-physiological shear stress induced platelet activation and function alternation. *Thromb Res*. 2022;219:141-149. doi:10.1016/j.thromres.2022.09.019

bioRxiv preprint doi: https://doi.org/10.64898/2026.10.26.761989; this version posted October 28, 2026. The copyright holder for this preprint (which was not certified by peer review) is the author/funder, who has granted bioRxiv a license to display the preprint in perpetuity. It is made available under a CC-BY-NC 4.0 International license.

16. Li W, Tu LN, Hsieh L, et al. A shear stress-responsive pathway in monocytes drives cardiopulmonary bypass-induced inflammation via spectrin/RAF1/store-operated calcium entry. *Cell Rep*. 2026;45(2):116903. doi:10.1016/j.celrep.2025.116903

17. Li W, Tu LN, Hsieh L, et al. Cardiopulmonary bypass activates classical monocytes via shear-mediated activation of Store-Operated Calcium Entry. *Cell Biology*. Preprint posted online May 5, 2022. doi:10.1101/2022.05.04.490549

18. De Somer F, Mulholland JW, Bryan MR, Aloisio T, Van Nooten GJ, Ranucci M. O2 delivery and CO2 production during cardiopulmonary bypass as determinants of acute kidney injury: time for a goal-directed perfusion management? *Crit Care*. 2011;15(4):R192. doi:10.1186/cc10349

19. Dreher M, Min J, Mavroudis C, et al. Indexed oxygen delivery during pediatric cardiopulmonary bypass is a modifiable risk factor for postoperative acute kidney injury. *J Extracorpor Technol*. 2023;55(3):112-120. doi:10.1051/ject/2023029

20. Gao P, Jin Y, Zhang P, Wang W, Hu J, Liu J. Nadir oxygen delivery is associated with postoperative acute kidney injury in low-weight infants undergoing cardiopulmonary bypass. *Front Cardiovasc Med*. 2022;9:1020846. doi:10.3389/fcvm.2022.1020846

21. Zhang Y, Wang B, Zhou XJ, Guo LJ, Zhou RH. Nadir Oxygen Delivery During Pediatric Bypass as a Predictor of Acute Kidney Injury. *Ann Thorac Surg*. 2022;113(2):647-653. doi:10.1016/j.athoracsur.2021.01.026

22. Hayward A, Robertson A, Thiruchelvam T, et al. Oxygen delivery in pediatric cardiac surgery and its association with acute kidney injury using machine learning. *J Thorac Cardiovasc Surg*. 2023;165(4):1505-1516. doi:10.1016/j.jtcvs.2022.05.039

bioRxiv preprint doi: https://doi.org/10.64898/2026.10.26.761989; this version posted October 28, 2026. The copyright holder for this preprint (which was not certified by peer review) is the author/funder, who has granted bioRxiv a license to display the preprint in perpetuity. It is made available under a CC-BY-NC 4.0 International license.

23. Jonas RA, Wypij D, Roth SJ, et al. The influence of hemodilution on outcome after hypothermic cardiopulmonary bypass: results of a randomized trial in infants. *J Thorac Cardiovasc Surg*. 2003;126(6):1765-1774. doi:10.1016/j.jtcvs.2003.04.003

24. Newburger JW, Jonas RA, Soul J, et al. Randomized trial of hematocrit 25% versus 35% during hypothermic cardiopulmonary bypass in infant heart surgery. *J Thorac Cardiovasc Surg*. 2008;135(2):347-354.e4. doi:10.1016/j.jtcvs.2007.01.051

25. Wypij D, Jonas RA, Bellinger DC, et al. The effect of hematocrit during hypothermic cardiopulmonary bypass in infant heart surgery: Results from the combined Boston hematocrit trials. *J Thorac Cardiovasc Surg*. 2008;135(2):355-360. doi:10.1016/j.jtcvs.2007.03.067

26. Ranucci M, Biagioli B, Scolletta S, et al. Lowest hematocrit on cardiopulmonary bypass impairs the outcome in coronary surgery: An Italian Multicenter Study from the National Cardioanesthesia Database. *Tex Heart Inst J*. 2006;33(3):300-305.

27. Tadphale SD, Ramakrishnan K, Spentzas T, et al. Impact of Different Cardiopulmonary Bypass Strategies on Renal Injury After Pediatric Heart Surgery. *Ann Thorac Surg*. 2021;111(4):1374-1379. doi:10.1016/j.athoracsur.2020.05.056

28. Ramakrishnan K, Kumar TS, Boston US, Allen J, Knott-Craig CJ. Cardiopulmonary bypass in neonates and infants: advantages of high flow high hematocrit bypass strategy—clinical practice review. *Transl Pediatr*. 2023;12(7):1431-1438. doi:10.21037/tp-23-94

29. Reagor JA, Clingan S, Gao Z, et al. Higher Flow on Cardiopulmonary Bypass in Pediatrics Is Associated With a Lower Incidence of Acute Kidney Injury. *Semin Thorac Cardiovasc Surg*. 2020;32(4):1015-1020. doi:10.1053/j.semtcvs.2019.08.007

bioRxiv preprint doi: https://doi.org/10.64898/2026.10.26.761989; this version posted October 28, 2026. The copyright holder for this preprint (which was not certified by peer review) is the author/funder, who has granted bioRxiv a license to display the preprint in perpetuity. It is made available under a CC-BY-NC 4.0 International license.

30. Jaffrin MY, Shapiro AH. Peristaltic Pumping. *Annu Rev Fluid Mech*. 1971;3(1):13-37. doi:10.1146/annurev.fl.03.010171.000305

31. Mulholland JW, Shelton JC, Luo XY. Blood flow and damage by the roller pumps during cardiopulmonary bypass. *J Fluids Struct*. 2005;20(1):129-140. doi:10.1016/j.jfluidstructs.2004.10.008

32. Zhou X, Liang XM, Zhao G, Su Y, Wang Y. A New Computational Fluid Dynamics Method for In-Depth Investigation of Flow Dynamics in Roller Pump Systems. *Artif Organs*. 2014;38(7). doi:10.1111/aor.12319

33. Zhou Y, Sun B, Chen M, Cui C. Research of flow dynamics and occlusion condition in roller pump systems used for ventricular assist. *Artif Organs*. 2021;45(1). doi:10.1111/aor.13790

34. Weinberg SL, Eckstein EC, Shapiro AH. An experimental study of peristaltic pumping. *J Fluid Mech*. 1971;49(3):461-479. doi:10.1017/S0022112071002209

35. Shapiro AH, Jaffrin MY, Weinberg SL. Peristaltic pumping with long wavelengths at low Reynolds number. *J Fluid Mech*. 1969;37(4):799-825. doi:10.1017/S0022112069000899

36. Moscato F, Colacino FM, Arabia M, Danieli GA. Pressure pulsation in roller pumps: A validated lumped parameter model. *Med Eng Phys*. 2008;30(9):1149-1158. doi:10.1016/j.medengphy.2008.02.007

37. McIntyre MP, Van Schoor G, Uren KR, Kloppers CP. Modelling the pulsatile flow rate and pressure response of a roller-type peristaltic pump. *Sens Actuators Phys*. 2021;325:112708. doi:10.1016/j.sna.2021.112708

38. Elabbasi N, Bergstrom J, Brown S. Fluid-Structure Interaction Analysis of a Peristaltic Pump. In: *Proceedings of the 2011 COMSOL Conference in Boston*. COMSOL;

bioRxiv preprint doi: https://doi.org/10.64898/2026.10.26.761989; this version posted October 28, 2026. The copyright holder for this preprint (which was not certified by peer review) is the author/funder, who has granted bioRxiv a license to display the preprint in perpetuity. It is made available under a CC-BY-NC 4.0 International license.

2011. Accessed September 8, 2026. https://www.comsol.com/paper/fluid-structure-interaction-analysis-of-a-peristaltic-pump-11574

39. Formato G, Romano R, Formato A, et al. Fluid–Structure Interaction Modeling Applied to Peristaltic Pump Flow Simulations. *Machines*. 2019;7(3):50. doi:10.3390/machines7030050

40. Gartili A, Lapinte V, Briou B, Caillol S. Valorization of CNSL as a Sustainable Solution for PVC Plasticization: A Comprehensive Study of Cardanol–Cardol Mixture. *J Am Oil Chem Soc*. 2025;102(8):1141-1157. doi:10.1002/aocs.12955

41. Long JA, Undar A, Manning KB, Deutsch S. Viscoelasticity of pediatric blood and its implications for the testing of a pulsatile pediatric blood pump. *ASAIO J*. 2005;51(5):563-566. doi:10.1097/01.mat.0000180353.12963.f2

42. Hashemi J, Patel B, Chatzizisis YS, Kassab GS. Study of Coronary Atherosclerosis Using Blood Residence Time. *Front Physiol*. 2021;12:625420. doi:10.3389/fphys.2021.625420

43. Himburg HA, Grzybowski DM, Hazel AL, LaMack JA, Li XM, Friedman MH. Spatial comparison between wall shear stress measures and porcine arterial endothelial permeability. *Am J Physiol-Heart Circ Physiol*. 2004;286(5):H1916-H1922. doi:10.1152/ajpheart.00897.2003

44. Leverett LB, Hellums JD, Alfrey CP, Lynch EC. Red blood cell damage by shear stress. *Biophys J*. 1972;12(3):257-273. doi:10.1016/S0006-3495(72)86085-5

45. Vercaemst L. Hemolysis in cardiac surgery patients undergoing cardiopulmonary bypass: a review in search of a treatment algorithm. *J Extra Corpor Technol*. 2008;40(4):257-267.

bioRxiv preprint doi: https://doi.org/10.64898/2026.10.26.761989; this version posted October 28, 2026. The copyright holder for this preprint (which was not certified by peer review) is the author/funder, who has granted bioRxiv a license to display the preprint in perpetuity. It is made available under a CC-BY-NC 4.0 International license.

633 46. Watanabe N, Arakawa Y, Sou A, et al. Deformability of human red blood cells
634 exposed to a uniform shear stress as measured by a cyclically reversing shear flow generator.
635 *Physiol Meas*. 2007;28(5):531-545. doi:10.1088/0967-3334/28/5/007

636 47. Williams DC, Turi JL, Hornik CP, et al. Circuit Oxygenator Contributes to
637 Extracorporeal Membrane Oxygenation–Induced Hemolysis. *ASAIO J*. 2015;61(2):190-195.
638 doi:10.1097/MAT.0000000000000173

639 48. Lawson S, Ellis C, McRobb C, Mejak B. Mechanical Aspects of Pediatric Cardio
640 Pulmonary Bypass. In: Da Cruz EM, Ivy D, Jaggers J, eds. *Pediatric and Congenital*
641 *Cardiology, Cardiac Surgery and Intensive Care*. Springer London; 2014:771-789.
642 doi:10.1007/978-1-4471-4619-3_75

643 49. Junior FUV, Antunes N, De Oliveira PP, Filho LMS, Vilarinho KAS, Costa ET. Does
644 the Roller Pump Adjustment in Cardiopulmonary Bypass Settings Influence Hemolysis? *Int J*
645 *Artif Organs*. 2017;40(3):118-122. doi:10.5301/ijao.5000570

646 50. Whiting D, Yuki K, DiNardo JA. Cardiopulmonary bypass in the pediatric
647 population. *Best Pract Res Clin Anaesthesiol*. 2015;29(2):241-256.
648 doi:10.1016/j.bpa.2015.03.006

649 51. Olia SE, Maul TM, Antaki JF, Kameneva MV. Mechanical Blood Trauma in Assisted
650 Circulation: Sublethal RBC Damage Preceding Hemolysis. *Int J Artif Organs*.
651 2016;39(4):150-159. doi:10.5301/ijao.5000478

652 52. Bhirowo YP, Raksawardana YK, Setianto BY, et al. Hemolysis and cardiopulmonary
653 bypass: meta-analysis and systematic review of contributing factors. *J Cardiothorac Surg*.
654 2023;18(1):291. doi:10.1186/s13019-023-02406-y

bioRxiv preprint doi: https://doi.org/10.64898/2026.10.26.761989; this version posted October 28, 2026. The copyright holder for this preprint (which was not certified by peer review) is the author/funder, who has granted bioRxiv a license to display the preprint in perpetuity. It is made available under a CC-BY-NC 4.0 International license.

655 53. Radley G, Laura Pieper I, Thomas BR, Hawkins K, Thornton CA. Artificial shear
656 stress effects on leukocytes at a biomaterial interface. *Artif Organs*. 2019;43(7).
657 doi:10.1111/aor.13409

658 54. Garcia-Herreros A, Yeh Y, Peng Z, Del Álamo JC. Cyclic Mechanical Stresses Alter
659 Erythrocyte Membrane Composition and Microstructure and Trigger Macrophage
660 Phagocytosis. *Adv Sci*. 2022;9(20):2201481. doi:10.1002/advs.202201481

661 55. Barbu M, Kolsrud O, Ricksten SE, et al. Dextran- Versus Crystalloid-Based Prime in
662 Cardiac Surgery: A Prospective Randomized Pilot Study. *Ann Thorac Surg*.
663 2020;110(5):1541-1547. doi:10.1016/j.athoracsur.2020.03.031

664 56. Morgan I. Superiority of centrifugal pump over roller pump in paediatric cardiac
665 surgery: prospective randomised trial. *Eur J Cardiothorac Surg*. 1998;13(5):526-532.
666 doi:10.1016/S1010-7940(98)00067-0

667 57. Ashraf SS, Tian Y, Cowan D, et al. Proinflammatory cytokine release during pediatric
668 cardiopulmonary bypass: influence of centrifugal and roller pumps. *J Cardiothorac Vasc*
669 *Anesth*. 1997;11(6):718-722. doi:10.1016/s1053-0770(97)90164-6

670 58. Andersen KS, Nygreen EL, Grong K, Leirvaag B, Holmsen H. Comparison of the
671 centrifugal and roller pump in elective coronary artery bypass surgery--a prospective,
672 randomized study with special emphasis upon platelet activation. *Scand Cardiovasc J SCJ*.
673 2003;37(6):356-362. doi:10.1080/14017430310015523

674 59. Halaweish I, Cole A, Cooley E, Lynch WR, Haft JW. Roller and Centrifugal Pumps:
675 A Retrospective Comparison of Bleeding Complications in Extracorporeal Membrane
676 Oxygenation. *ASAIO J*. 2015;61(5):496-501. doi:10.1097/MAT.0000000000000243

bioRxiv preprint doi: https://doi.org/10.64898/2026.10.26.761989; this version posted October 28, 2026. The copyright holder for this preprint (which was not certified by peer review) is the author/funder, who has granted bioRxiv a license to display the preprint in perpetuity. It is made available under a CC-BY-NC 4.0 International license.

677 60. Pozrikidis C. A study of peristaltic flow. *J Fluid Mech*. 1987;180:515-527.
678 doi:10.1017/S0022112087001939

679 61. Li M, Brasseur JG. Non-steady peristaltic transport in finite-length tubes. *J Fluid*
680 *Mech*. 1993;248:129-151. doi:10.1017/S0022112093000710

681 62. Boettcher W, Sinzobahamvya N, Miera O, et al. Routine Application of Bloodless
682 Priming in Neonatal Cardiopulmonary Bypass: A 3-Year Experience. *Pediatr Cardiol*.
683 2017;38(4):807-812. doi:10.1007/s00246-017-1585-x

684 63. Bohuta L, Chan T, Charette K, et al. Significant reduction in blood product usage,
685 same early outcomes: Blood conservation in infants undergoing open heart surgery. *JTCVS*
686 *Open*. 2024;22:450-457. doi:10.1016/j.xjon.2024.10.006

687 64. Bateson B, Ange B, Doddala B, Hazenberg E, Bohuta L, St. Louis J. Use and
688 Outcomes Associated With a Clear Prime for Infants Undergoing Cardiac Surgery. *Ann*
689 *Thorac Surg Short Rep*. 2026;4(3):863-867. doi:10.1016/j.atssr.2026.02.024

690 65. Boettcher W, Schulz A, Sinzobahamvya N, et al. Coagulation Profile of Neonates
691 Undergoing Arterial Switch Surgery With Crystalloid Priming of the Cardiopulmonary
692 Bypass Circuit. *J Cardiothorac Vasc Anesth*. 2022;36(6):1598-1605.
693 doi:10.1053/j.jvca.2021.08.006

694 66. Tamari Y, Lee-Sensiba K, Leonard EF, Tortolani AJ. A Dynamic Method for Setting
695 Roller Pumps Nonocclusively Reduces Hemolysis and Predicts Retrograde Flow: *ASAIO J*.
696 1997;43(1):39-52. doi:10.1097/00002480-199743010-00009

697 67. Huang PY, Hellums JD. Aggregation and disaggregation kinetics of human blood
698 platelets: Part II. Shear-induced platelet aggregation. *Biophys J*. 1993;65(1):344-353.
699 doi:10.1016/S0006-3495(93)81079-8

bioRxiv preprint doi: https://doi.org/10.64898/2026.10.26.761989; this version posted October 28, 2026. The copyright holder for this preprint (which was not certified by peer review) is the author/funder, who has granted bioRxiv a license to display the preprint in perpetuity. It is made available under a CC-BY-NC 4.0 International license.

68. Fraser KH, Zhang T, Taskin ME, Griffith BP, Wu ZJ. A Quantitative Comparison of Mechanical Blood Damage Parameters in Rotary Ventricular Assist Devices: Shear Stress, Exposure Time and Hemolysis Index. *J Biomech Eng*. 2012;134(8):081002. doi:10.1115/1.4007092

69. Rossini L, Braun OÖ, Brambatti M, et al. Intraventricular Flow Patterns in Patients Treated with Left Ventricular Assist Devices. *ASAIO J*. 2021;67(1):74-83. doi:10.1097/MAT.0000000000001158

70. Alemu Y, Bluestein D. Flow-induced Platelet Activation and Damage Accumulation in a Mechanical Heart Valve: Numerical Studies. *Artif Organs*. 2007;31(9):677-688. doi:10.1111/j.1525-1594.2007.00446.x

71. Waldrop L, Miller L. Large-amplitude, short-wave peristalsis and its implications for transport. *Biomech Model Mechanobiol*. 2016;15(3):629-642. doi:10.1007/s10237-015-0713-x

72. Guerrelli D, Desai M, Semaan Y, et al. Prevalence and clinical implications of heightened plastic chemical exposure in pediatric patients undergoing cardiopulmonary bypass. *Transfusion (Paris)*. 2024;64(5):808-823. doi:10.1111/trf.17821

73. Spiwak AJB, Horbal A, Leatherbury R, Hansford DJ. Extracorporeal tubing in the roller pump raceway: physical changes and particulate generation. *J Extra Corpor Technol*. 2008;40(3):188-192.

74. Peek GJ, Wong K, Morrison C, Killer HM, Firmin RK. Tubing failure during prolonged roller pump use: a laboratory study. *Perfusion*. 1999;14(6):443-452. doi:10.1177/026765919901400607

bioRxiv preprint doi: https://doi.org/10.64898/2026.10.26.761989; this version posted October 28, 2026. The copyright holder for this preprint (which was not certified by peer review) is the author/funder, who has granted bioRxiv a license to display the preprint in perpetuity. It is made available under a CC-BY-NC 4.0 International license.

722 75. Snyder EJ, McElwee DL, Harb HM, et al. Investigation of Fatigue Failure of S-65-HL
723 "Super Tygon" Roller Pump Tubing. *J Extracorpor Technol*. 1996;28(2):79-87.
724 doi:10.1051/ject/199628279

725

726

bioRxiv preprint doi: https://doi.org/10.64898/2026.10.26.761989; this version posted October 28, 2026. The copyright holder for this preprint (which was not certified by peer review) is the author/funder, who has granted bioRxiv a license to display the preprint in perpetuity. It is made available under a CC-BY-NC 4.0 International license.

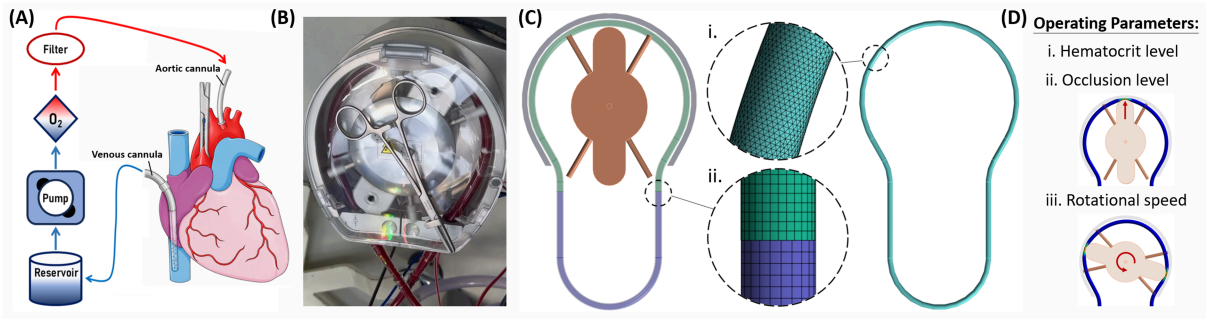
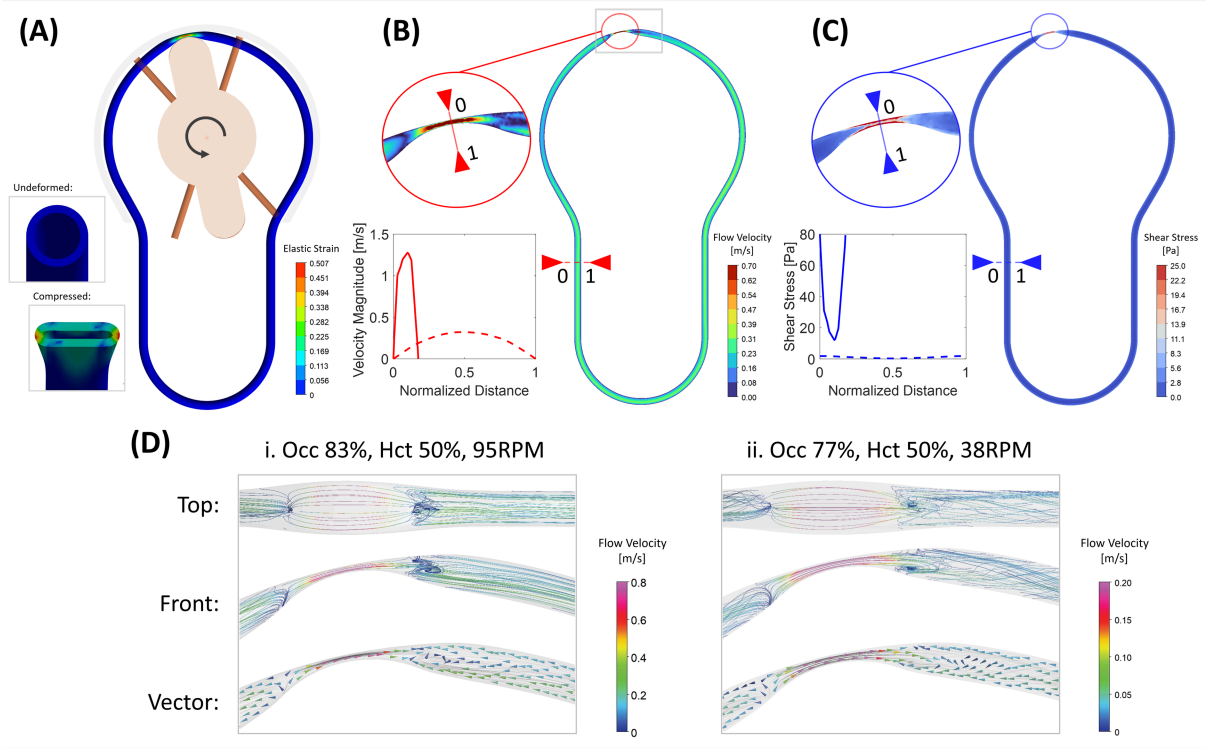


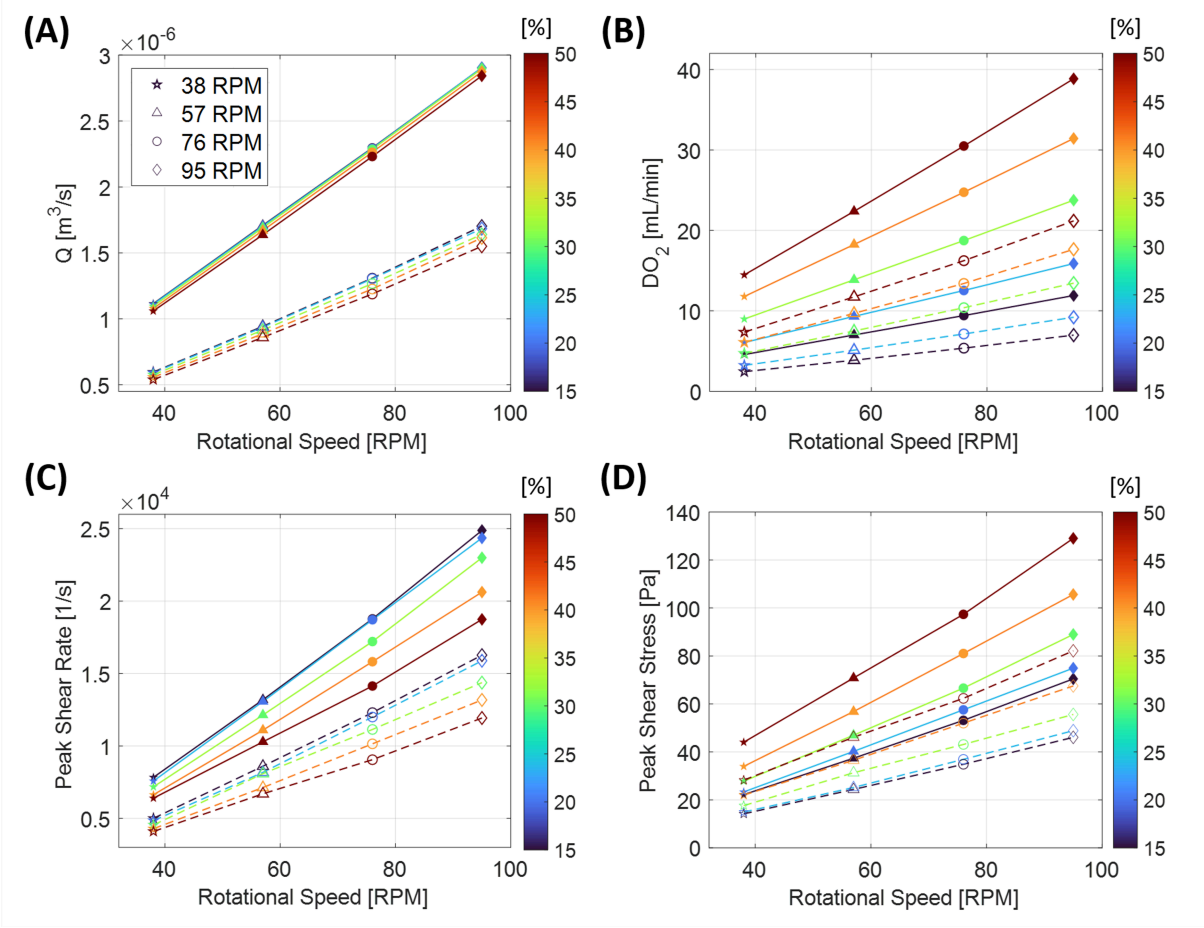
Figure 1. Roller pump cardiopulmonary bypass (RP-CPB) circuit, pump geometry, computational model construction, and investigated operating parameters. **(A)** Simplified schematic of the RP-CPB circuit. **(B)** LivaNova S5 Roller Pump used as the basis for model construction. **(C)** Computational model including solid-domain assembly (left) and closed-loop fluid domain (right). Insets show **(i)** the unstructured tetrahedral fluid mesh and **(ii)** the bonded interface between the deformable (green) and fixed (purple) tubing segments. **(D)** Investigated operating parameters: **(i)** hematocrit levels of 15%-50%, **(ii)** roller occlusion levels of 77% and 83%, and **(iii)** rotational speeds of 38-95 rpm.



bioRxiv preprint doi: https://doi.org/10.64898/2026.10.26.761989; this version posted October 28, 2026. The copyright holder for this preprint (which was not certified by peer review) is the author/funder, who has granted bioRxiv a license to display the preprint in perpetuity. It is made available under a CC-BY-NC 4.0 International license.

738 **Figure 2. Roller compression generates localized high shear, backflow, and recirculation.**
739 Results of ϕ= 83%, Hct=50%, Ω= 95 rpm are shown at peak shear stress. **(A)** Equivalent elastic
740 strain in the deforming tubing; insets show the undeformed and compressed tubing cross-
741 sectional geometry. **(B, C)** Velocity and shear stress on the same cross-sectional plane,
742 respectively; insets show each field within the occluded region and corresponding profiles
743 across the compressed gap and free tubing. **(D)** Velocity-colored streamlines and vector maps
744 near the occlusion for **(i)** ϕ=83%, Hct=50%, Ω=95 rpm and **(ii)** ϕ=77%, Hct=50%, Ω=38 rpm,
745 illustrating how backward gap flow interacts with forward bulk transport to produce stagnation
746 and recirculation.

747

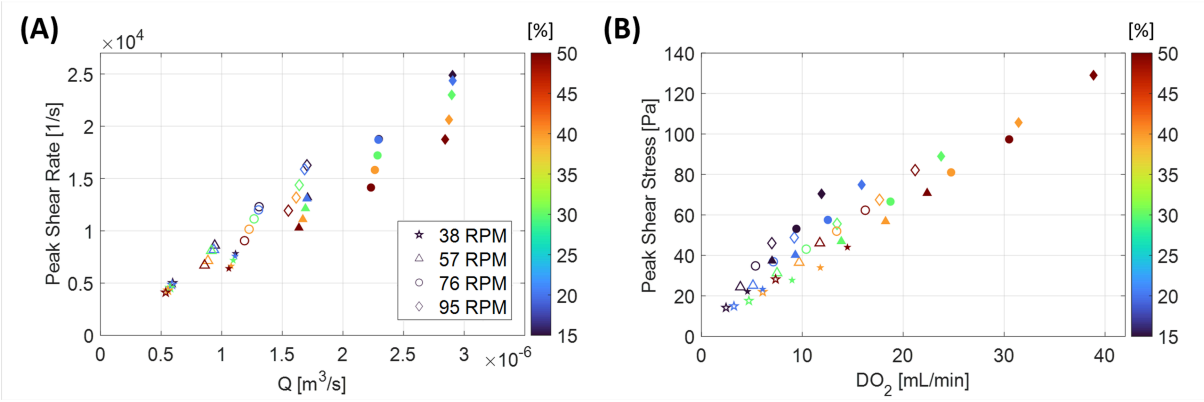


748

bioRxiv preprint doi: https://doi.org/10.64898/2026.10.26.761989; this version posted October 28, 2026. The copyright holder for this preprint (which was not certified by peer review) is the author/funder, who has granted bioRxiv a license to display the preprint in perpetuity. It is made available under a CC-BY-NC 4.0 International license.

749 **Figure 3. Effects of CPB operating conditions on cycle-averaged flow transport, oxygen**
750 **delivery, and flow shear. (A)** Cycle-averaged volumetric flow rate ($\underline{Q}$ [m^3/s]), **(B)** oxygen
751 delivery (DO_2 [mL/min]), **(C)** peak shear rate [s^{-1}], and **(D)** peak shear stress [Pa] as functions
752 of roller rotational speed (Ω, rpm) under combinations of two occlusion levels (77% and 83%;
753 open and filled symbols, respectively), four rotational speeds (38, 57, 76, and 95 rpm; symbol
754 shapes), and hematocrit levels ranging from 15% to 50% (symbol color). Trend lines connect
755 cases with fixed hematocrit and occlusion to illustrate the dependence of each metric on Ω
756 (dashed and solid lines represent 77% and 83% occlusion, respectively).

757

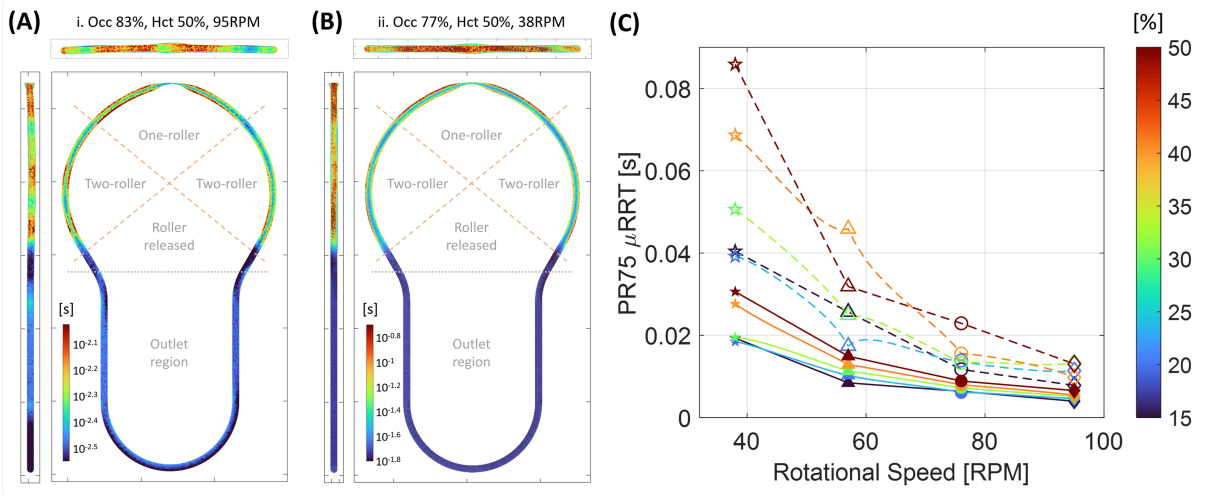


758

759 **Figure 4. Relationships between flow rate, oxygen delivery, and flow shear across CPB**
760 **operating conditions**. **(A)** Cycle-averaged peak shear rate ($\underline{S_{max}}$, s^{-1}) vs. flow rate, ($\underline{Q}$, m^3/s).
761 **(B)** Cycle-averaged peak shear stress ($\underline{\tau_{max}}$, Pa) vs. oxygen delivery (DO_2, mL/min). Symbol
762 shape denotes roller rotational speed (rpm), symbol color indicates hematocrit level, and open
763 and filled symbols represent 77% and 83% occlusion, respectively.

764

bioRxiv preprint doi: https://doi.org/10.64898/2026.10.26.761989; this version posted October 28, 2026. The copyright holder for this preprint (which was not certified by peer review) is the author/funder, who has granted bioRxiv a license to display the preprint in perpetuity. It is made available under a CC-BY-NC 4.0 International license.



765

766 **Figure 5. Spatial distribution and parametric dependence of relative residence time. (A,**
767 **B)** Front, top, and side view maps of μRRT (s) at the tubing wall for the same representative
768 operating conditions shown in Figure 2D: (A) 83% occlusion, 50% hematocrit, and 95 rpm; (B)
769 77% occlusion, 50% hematocrit, and 38 rpm. The gray dashed line separates the raceway and
770 free tubing segments. Within the raceway, the upper, lateral and lower quadrants correspond
771 respectively to one-roller contact, two-roller contact, and roller release. A logarithmic
772 colormap was used to aid visualization. **(C)** 75th percentile of μRRT within the raceway (PR75,
773 s) vs. rotational speed (Ω, rpm). Symbol color denotes hematocrit; open and filled symbols
774 represent 77% and 83% occlusion, respectively.

775

bioRxiv preprint doi: https://doi.org/10.64898/2026.10.26.761989; this version posted October 28, 2026. The copyright holder for this preprint (which was not certified by peer review) is the author/funder, who has granted bioRxiv a license to display the preprint in perpetuity. It is made available under a CC-BY-NC 4.0 International license.

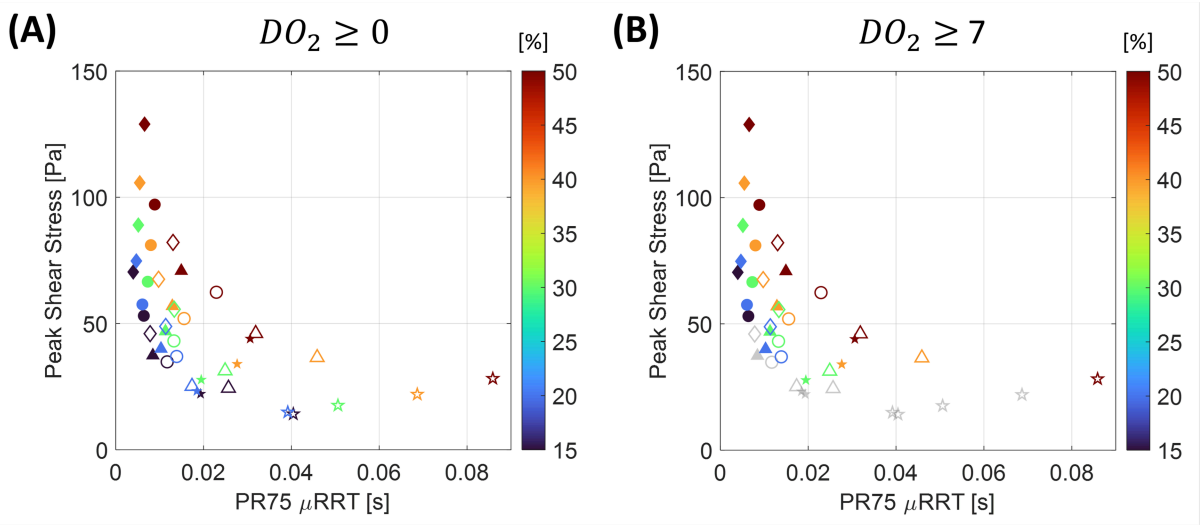
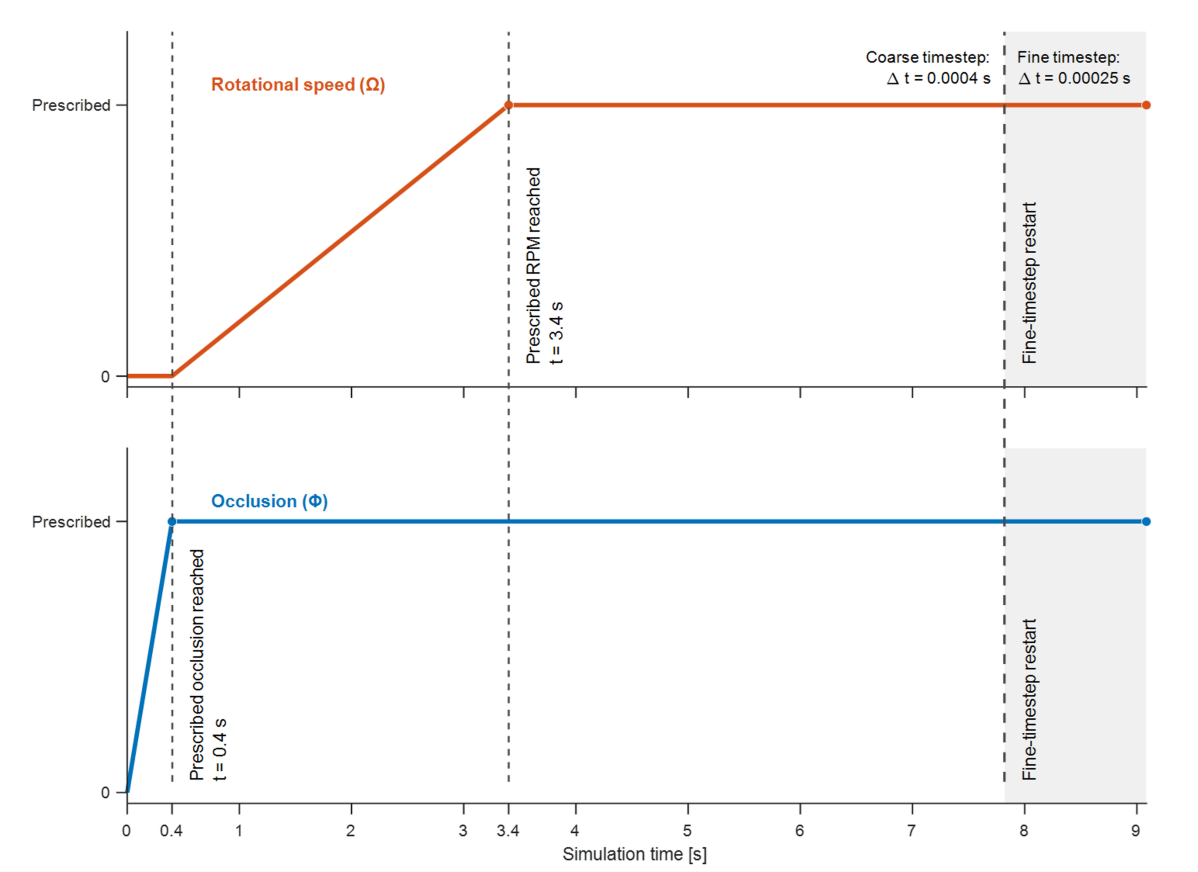


Figure 6. Trade-off between peak shear stress and relative residence time. **(A)** Cycle-averaged peak shear stress ($\underline{\tau}_{max}$, Pa) vs. the 75th percentile of μRRT within the raceway (PR75, s). **(B)** Same plot after applying an oxygen-delivery filter ($DO_2 \geq 7$ mL/min), with operating conditions below the threshold shown in gray. Symbol shape denotes roller rotational speed, symbol color denotes hematocrit level, and open and filled symbols represent 77% and 83% occlusion, respectively, consistent with previous figures.

bioRxiv preprint doi: https://doi.org/10.64898/2026.10.26.761989; this version posted October 28, 2026. The copyright holder for this preprint (which was not certified by peer review) is the author/funder, who has granted bioRxiv a license to display the preprint in perpetuity. It is made available under a CC-BY-NC 4.0 International license.



Supplementary Figure 1. Prescribed roller motion and simulation time-stepping sequence. Initial roller engagement establishes the target tubing occlusion during 0–0.4 s. Angular speed then increases linearly from zero to the prescribed value during 0.4–3.4 s, followed by constant-speed rotation. Vertical dashed lines mark completion of initial engagement, attainment of the prescribed angular speed, and the fine-timestep restart. The shaded region indicates the fine-timestep simulation interval; the restart time varies by case. Ω, angular speed; Φ, occlusion; Δt, simulation time step.